# On the Benefits of In-Flight System Identification for Autonomous Airdrop Systems

Michael Ward* and Mark Costello†
*Georgia Institute of Technology, Atlanta, Georgia 30332*
and
Nathan Slegers‡
*University of Alabama in Huntsville, Huntsville, Alabama 35899*

A unique feature of airdrop systems is the inherent and large variability in flight dynamic characteristics. The same physical article dropped on two different occasions will exhibit significantly different dynamic response. The problem only becomes worse for different test articles. Control systems for autonomous airdrop systems explicitly or implicitly assume knowledge of the flight dynamic characteristics in some way, shape, or form. A question facing autonomous airdrop designers is whether to use precomputed dynamic characteristics inside the control law, or to compute the needed flight dynamic characteristics in-flight and subsequently employ them in the control law. This paper establishes conditions when in-flight identified characteristics, with a focus on the turn rate dynamics, should be used, and when it is better to use precomputed results. It is shown that with expected levels of system variability, sensor noise, and atmospheric wind, in-flight identification generally produces significantly more accurate dynamic behavior of the lateral dynamics than a precomputed model of the nominal system, even when the in-flight identification is performed with highly inaccurate sensor data. The only exception to this rule observed in this work is the situation where atmospheric winds are high and a direct heading measurement is not available. In this situation, a precomputed estimate of the time constant of the lateral dynamics is more accurate than an in-flight estimate. These conclusions are reached though a comprehensive simulation study using a validated airdrop flight dynamic model applied to both a small and large parafoil.

## Nomenclature

| | | |
|---|---|---|
| $A, B, C,$ $P, Q, R$ | = | apparent mass and inertia coefficients |
| $b$ | = | canopy span |
| $C_{D,P}$ | = | payload drag coefficient |
| $C_{L,i}, C_{D,i}$ | = | lift and drag coefficients of the $i$th canopy element |
| $d$ | = | canopy arc radius |
| $[I]$ | = | identity matrix |
| $[I_T]$ | = | total system inertia matrix |
| $L_{AM}, M_{AM},$ $N_{AM}$ | = | components of apparent mass moment in the body reference frame |
| $m$ | = | total system mass |
| $p, q, r$ | = | angular velocity components expressed in the body reference frame |
| $[S_x^B]$ | = | skew symmetric cross product matrix for vector $x$ in body frame |
| $[S_\omega^B]$ | = | skew symmetric cross product matrix for system angular velocity |
| $[S_{cg,i}^B]$ | = | skew symmetric cross product matrix for distance vector from system center of gravity to $i$th canopy element |
| $[S_{cg,M}^B]$ | = | skew symmetric cross product matrix for distance vector from system center of gravity to apparent mass reference point |
| $[S_{cg,P}^B]$ | = | skew symmetric cross product matrix for distance vector from system center of gravity to payload |
| $S_C, S_P, S_i$ | = | canopy, payload, and canopy element reference areas |
| $u, v, w$ | = | velocity components of system mass center expressed in body frame |
| $\tilde{u}_i, \tilde{v}_i, \tilde{w}_i$ | = | aerodynamic velocity components of $i$th canopy element in $i$th canopy frame |
| $\mathbf{V}$ | = | projection of velocity vector on horizontal plane |
| $\mathbf{V}_0$ | = | projection of velocity vector on horizontal plane in wind-fixed frame |
| $\mathbf{V}_w$ | = | wind vector |
| $X_{A,i}, Y_{A,i},$ $Z_{A,i}$ | = | components of aerodynamic force on $i$th canopy element in body frame |
| $X_{A,P}, Y_{A,P},$ $Z_{A,P}$ | = | components of aerodynamic force on payload in body frame |
| $X_{AM}, Y_{AM},$ $Z_{AM}$ | = | components of apparent mass force in body frame |
| $X_W, Y_W, Z_W$ | = | components of weight vector in body frame |
| $x, y$ | = | north and east position |
| $\beta$ | = | sideslip angle |
| $\Lambda$ | = | canopy arc angular span |
| $\delta_L, \delta_R$ | = | normalized left and right brake deflections |
| $\tau$ | = | azimuthal rate time constant |
| $\tau_e$ | = | correlated measurement noise time constant |
| $\phi, \theta, \psi$ | = | Euler roll, pitch, and yaw angles |
| $\chi$ | = | azimuth angle (course over ground) |
| $\chi_0$ | = | wind-relative azimuth angle (course in wind-fixed frame) |
| $\dot{\chi}_{0,ss}$ | = | steady-state wind-relative azimuthal rate |
| $\psi_w$ | = | wind vector heading angle |

*Graduate Research Assistant, School of Aerospace Engineering. Member AIAA.
†Sikorsky Associate Professor, School of Aerospace Engineering. Associate Fellow AIAA.
‡Assistant Professor, Department of Mechanical and Aerospace Engineering. Member AIAA.

## I. Introduction

AUTONOMOUS guided parafoils are an attractive option for payload delivery due to their low weight and packing volume and their ability to penetrate winds and maneuver to achieve high

placement accuracy. These systems require an onboard guidance, navigation, and control system to generate and track a desired path to the target. Either directly or indirectly, current autonomous airdrop system control laws contain an embedded model of the flight dynamics that is loaded into the automatic guidance unit (AGU) before each flight [1–8]. In the case of model predictive control, the controller contains the actual dynamic model, but in the more traditional control schemes the model is embedded in the form of the preselected control gains and logic gates. For control system design purposes, a flight dynamic model is typically created from analytical modeling or a best fit to flight data [9–12]. A unique feature of parafoil and payload aircraft is the high degree of variability of the basic flight dynamics from drop to drop, particularly the control response. Parafoil canopies made to the same specifications will exhibit some variation in canopy and rigging geometry, and the weight and geometry of the payload will change from drop to drop. Furthermore, airdrop systems are susceptible to preflight programming errors (such as specifying an incorrect payload weight or canopy), rigging errors (such as control line or riser adjustment), and deployment malfunctions (such as partially inflated or torn canopies and twisted rigging lines). Even with no apparent malfunctions, the same parafoil and payload system will often tend to exhibit a significantly different control bias with every drop. This means that the nominal or average model will differ substantially from the actual flight dynamics, and this can induce substantial degradations in path tracking ability and subsequently landing accuracy.

A solution to the above problem is to identify the needed dynamic and control characteristics in-flight using a system identification algorithm. A significant literature database on parafoil and payload aircraft system identification has been reported including estimation of flight dynamic models and atmospheric wind velocity. While most of this work has focused on batch processing, some work is directed toward in-flight estimation [1,2,5,6]. The key quantities to estimate for autonomous parafoil and payload aircraft are the atmospheric wind velocity vector and the lateral control response. Atmospheric wind estimation is obtained by subtracting an estimate of the wind-relative velocity vector from the observed ground track velocity [1–5]. Airspeed of the airdrop system is assumed known from a preflight analysis. Preflight models include a constant assumed airspeed [5], airspeed determined from a constant reference dynamic pressure [13], and airspeed determined from a constant reference glide slope and measured sink rate [6]. Jann developed a nonlinear filter for simultaneous estimation of the wind and airspeed using Global Positioning System (GPS) data [5], though the effectiveness of the filter in estimating airspeed is not mentioned specifically. Calise and Preston pointed out that it is simple to obtain an airspeed estimate from GPS data by flying a complete circle, though they do not perform this maneuver in every flight [2]. Beyond wind and airspeed determination, transient and steady-state lateral control characteristics are estimated. Calise and Preston developed an adaptive stability augmentation system for guided parafoils and demonstrated the effectiveness of the approach in simulation [1,2]. Their approach identifies a set of reference dynamics for a particular system and then applies an adaptive correction to account for flight-to-flight variability in the system dynamics. This approach requires high quality measurements and has led them to pursue a control scheme based on bank angle feedback using a GPS/inertial measurement unit combination rather than traditional heading angle/heading rate feedback.

If the system identification task is performed in-flight, the controller can be designed online so that it is always tuned to the actual flight dynamics. While this is advantageous, it is not without problems. Any system identification scheme requires measurement of appropriate control inputs and response outputs to estimate air vehicle properties. While autonomous airdrop systems already incorporate a sensor suite for feedback control, the sensor suite required for system identification requires more accurate measurement of more vehicle states than the sensor suite required for flight control. Also, errors associated with sensors can be sufficiently large to render estimation of dynamic characteristics inaccurate. On the other hand, dynamic characteristics generated before flight from

analysis and prior flight testing do not have sensor requirements, but are not capable of adapting to the peculiar dynamics of each dropped item. The purpose of the current article is to explore the tradeoff between precomputed and preloaded dynamic characteristics versus in-flight estimated characteristics. The approach presented here is meant to be generally applicable in that it does not depend on specific guidance, navigation, and control strategies.

Toward this end, a straightforward and robust prototype procedure to perform the entire system identification task in-flight is defined. The procedure is based on using an extended Kalman filter observer to estimate the wind-relative azimuth angle and rate in-flight. The process is demonstrated with simulated measurements for a GPS unit operating alone and a GPS unit and heading measurement combination. Windows of estimated azimuthal rate data from a few key flight segments are then used to generate a model of the lateral dynamics. To compare the differences between use of precomputed models and in-flight estimated models, a 6 degrees of freedom, nonlinear parafoil and payload flight dynamic model is employed. Appropriate levels of uncertainty are injected into the dynamic model to represent drop to drop variability in the basic vehicle dynamics and appropriate levels of atmospheric wind are also injected into the simulation. Sensor noise and bias are added to the simulation data that is fed into the in-flight estimation algorithm to simulate low-cost, commercially available sensors. Results are generated for two exemplar systems, namely, a microparafoil flight tested by Slegers et al. [14] and the Airborne Systems 30k Megafly [15]. These systems have a total weight of approximately 5 and 30,000 lb, respectively. These systems were chosen to demonstrate that the in-flight system identification procedure is applicable to airdrop systems of any scale with minimal modifications. Example results are given to demonstrate the ability of the observer to estimate the wind and wind-relative dynamics. A Monte Carlo simulation is performed to evaluate the benefits of in-flight system identification with expected levels of sensor noise and variation in the parafoil and payload system. Results are presented in terms of the quality of the estimated characteristics rather than in terms of overall performance measures such as landing accuracy to preserve the separation of the methods described here from any particular guidance, navigation, and control strategies. The sensitivity of these results to changes in the assumed levels of sensor noise, system variation, and wind levels is studied to enable statements to be made regarding when it is most appropriate to use precomputed dynamic characteristics and when it is most appropriate to use in-flight estimation of dynamic characteristics.

## II.　Parafoil Dynamic Simulation Model

This section describes the nonlinear simulation model of the parafoil and payload system used to generate the simulated measurements that serve as inputs to the system identification process. The simulation model described here is not part of the linear dynamic model identified in-flight.

The combined system of the parafoil canopy and the payload are modeled with 6 degrees of freedom, including three inertial position components of the total system mass center as well as the three Euler orientation angles. With the exception of movable parafoil brakes, the parafoil canopy is considered to be a fixed shape. Canopy aerodynamics are modeled by splitting the canopy into five discrete elements as shown in Fig. 1 and determining the lift and drag on each element based on the local angle of attack. This aerodynamic model is a simple way of simulating a parafoil canopy. The lift and drag coefficients are not varied across the span. The lift and drag coefficients are set to match steady-state longitudinal data from flight tests, and the canopy arc is matched to the actual system geometries so that the orientation of the panels produces the aerodynamic moments and side force.

The kinematic equations for the parafoil and payload system are provided in Eqs. (1) and (2). A shorthand notation for trigonometric functions is employed where $\sin(x) = s_x$, $\cos(x) = c_x$, and $\tan(x) = t_x$.

$$\left\{ \begin{array}{c} \dot{x} \\ \dot{y} \\ \dot{z} \end{array} \right\} = [T_{IB}]^T \left\{ \begin{array}{c} u \\ v \\ w \end{array} \right\} \tag{1}$$
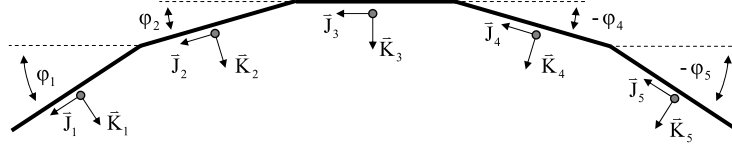
**Fig. 1 Canopy schematic.**

$$\left\{ \begin{array}{c} \dot{\phi} \\ \dot{\theta} \\ \dot{\psi} \end{array} \right\} = \begin{bmatrix} 1 & s_\phi t_\theta & c_\phi t_\theta \\ 0 & c_\phi & -s_\phi \\ 0 & s_\phi/c_\theta & c_\phi/c_\theta \end{bmatrix} \left\{ \begin{array}{c} p \\ q \\ r \end{array} \right\} \qquad (2)$$

The matrix $[T_{IB}]$ represents the transformation matrix from the inertial reference frame to the body reference frame

$$[T_{IB}] = \begin{bmatrix} c_\theta c_\psi & c_\theta s_\psi & -s_\theta \\ s_\phi s_\theta c_\psi - c_\phi s_\psi & s_\phi s_\theta s_\psi + c_\phi c_\psi & s_\phi c_\theta \\ c_\phi s_\theta c_\psi + s_\phi s_\psi & c_\phi s_\theta s_\psi - s_\phi c_\psi & c_\phi c_\theta \end{bmatrix} \qquad (3)$$

The dynamic equations are formed by summing forces and moments about the system center of gravity, both in the body reference frame, and equating to the time derivative of linear and angular momentum, respectively

$$m\left( \left\{ \begin{array}{c} \dot{u} \\ \dot{v} \\ \dot{w} \end{array} \right\} + [S_\omega^B]\left\{ \begin{array}{c} u \\ v \\ w \end{array} \right\} \right) = \left\{ \begin{array}{c} X_W \\ Y_W \\ Z_W \end{array} \right\} + \left\{ \begin{array}{c} X_{AM} \\ Y_{AM} \\ Z_{AM} \end{array} \right\}$$

$$+ \left\{ \begin{array}{c} X_{A,P} \\ Y_{A,P} \\ Z_{A,P} \end{array} \right\} + \sum_i \left\{ \begin{array}{c} X_{A,i} \\ Y_{A,i} \\ Z_{A,i} \end{array} \right\} \qquad (4)$$

$$[I_T]\left\{ \begin{array}{c} \dot{p} \\ \dot{q} \\ \dot{r} \end{array} \right\} + [S_\omega^B][I_T]\left\{ \begin{array}{c} p \\ q \\ r \end{array} \right\} = \left\{ \begin{array}{c} L_{AM} \\ M_{AM} \\ N_{AM} \end{array} \right\} + [S_{cg,M}^B]\left\{ \begin{array}{c} X_{AM} \\ Y_{AM} \\ Z_{AM} \end{array} \right\}$$

$$+ [S_{cg,P}^B]\left\{ \begin{array}{c} X_{A,P} \\ Y_{A,P} \\ Z_{A,P} \end{array} \right\} + \sum_i [S_{cg,i}^B]\left\{ \begin{array}{c} X_{A,i} \\ Y_{A,i} \\ Z_{A,i} \end{array} \right\} \qquad (5)$$

$S$ is the skew symmetric operator, used to express the cross product of two vectors as a matrix multiplication of the components of the vectors in a specified frame. For example, if the vectors **a**, **b**, and **c** are expressed in terms of their components in frame $B$

$$\mathbf{c} = \mathbf{a} \times \mathbf{b} \leftrightarrow \left\{ \begin{array}{c} c_x \\ c_y \\ c_z \end{array} \right\} = \begin{bmatrix} 0 & -a_z & a_y \\ a_z & 0 & -a_x \\ -a_y & a_x & 0 \end{bmatrix} \left\{ \begin{array}{c} b_x \\ b_y \\ b_z \end{array} \right\}$$

$$= [S_a^B]\left\{ \begin{array}{c} b_x \\ b_y \\ b_z \end{array} \right\} \qquad (6)$$

Forces appearing in Eq. (4) have contributions from weight, aerodynamic loads on the canopy and payload, and apparent mass. The weight contribution is given in Eq. (7)

$$\left\{ \begin{array}{c} X_W \\ Y_W \\ Z_W \end{array} \right\} = mg\left\{ \begin{array}{c} -s_\theta \\ s_\phi c_\theta \\ c_\phi c_\theta \end{array} \right\} \qquad (7)$$

Defining the transformation from the body frame to the frame attached to the $i$th element of the canopy as $[T_{B,i}]$ and defining the

wind velocity components in the inertial frame as $\{V_{W,x}, V_{W,y}, V_{W,z}\}^T$, the aerodynamic velocity of the $i$th element is given by Eq. (8). The aerodynamic velocity of the payload is given by the same equation with the body frame to element transformation equal to the identity matrix

$$\left\{ \begin{array}{c} \tilde{u}_i \\ \tilde{v}_i \\ \tilde{w}_i \end{array} \right\} = [T_{B,i}]\left( \left\{ \begin{array}{c} u \\ v \\ w \end{array} \right\} - [S_{cg,i}^B]\left\{ \begin{array}{c} p \\ q \\ r \end{array} \right\} - [T_{IB}]\left\{ \begin{array}{c} V_{W,x} \\ V_{W,y} \\ V_{W,z} \end{array} \right\} \right) \qquad (8)$$

The aerodynamic forces on the canopy elements are expressed in terms of lift and drag coefficients, which are functions of the angle of attack of each element $\alpha_i = \tan^{-1}(\tilde{w}_i/\tilde{u}_i)$ and the brake deflections $\delta_i$ if a brake spans the element, as shown in Eqs. (9) and (10). Equation (11) defines the canopy aerodynamic forces in the body reference frame

$$C_{L,i} = C_{L0,i} + C_{L\alpha,i}\alpha_i + C_{L\alpha3,i}\alpha_i^3 + C_{L\delta,i}\delta_i \qquad (9)$$

$$C_{D,i} = C_{D0,i} + C_{D\alpha2,i}\alpha_i^2 + C_{D\delta,i}\delta_i \qquad (10)$$

$$\left\{ \begin{array}{c} X_{A,i} \\ Y_{A,i} \\ Z_{A,i} \end{array} \right\} = \frac{1}{2}\rho S_i [T_{B,i}]^T \left( C_{L,i}\sqrt{\tilde{u}_i^2 + \tilde{w}_i^2}\left\{ \begin{array}{c} \tilde{w}_i \\ 0 \\ -\tilde{u}_i \end{array} \right\} \right.$$

$$\left. - C_{D,i}\sqrt{\tilde{u}_i^2 + \tilde{v}_i^2 + \tilde{w}_i^2}\left\{ \begin{array}{c} \tilde{u}_i \\ \tilde{v}_i \\ \tilde{w}_i \end{array} \right\} \right) \qquad (11)$$

The aerodynamic force on the payload consists entirely of profile drag and is given by Eq. (12)

$$\left\{ \begin{array}{c} X_{A,P} \\ Y_{A,P} \\ Z_{A,P} \end{array} \right\} = -\frac{1}{2}\rho S_P C_{D,P}\sqrt{\tilde{u}_P^2 + \tilde{v}_P^2 + \tilde{w}_P^2}\left\{ \begin{array}{c} \tilde{u}_P \\ \tilde{v}_P \\ \tilde{w}_P \end{array} \right\} \qquad (12)$$

Parafoils with small mass to volume ratios can experience large forces and moments from accelerating fluid. These are termed apparent mass effects. A precise accounting of these effects can substantially complicate the dynamic equations [14], but it is possible to obtain a good approximation of the effects with only a few of the terms. The approximate forms used for the apparent mass forces and moments are given in Eqs. (13) and (14). Parametric approximations given by Lissaman and Brown [16] are used to determine the apparent mass and inertia coefficients in Eq. (15)

$$\left\{ \begin{array}{c} X_{AM} \\ Y_{AM} \\ Z_{AM} \end{array} \right\} = -[I_{AM}]\left( \left\{ \begin{array}{c} \dot{u} \\ \dot{v} \\ \dot{w} \end{array} \right\} - [S_{cg,M}^B]\left\{ \begin{array}{c} \dot{p} \\ \dot{q} \\ \dot{r} \end{array} \right\} \right) \qquad (13)$$

$$\left\{ \begin{array}{c} L_{AM} \\ M_{AM} \\ N_{AM} \end{array} \right\} = -[I_{AI}]\left\{ \begin{array}{c} \dot{p} \\ \dot{q} \\ \dot{r} \end{array} \right\} \qquad (14)$$

$$[I_{AM}] = \begin{bmatrix} A & 0 & 0 \\ 0 & B & 0 \\ 0 & 0 & C \end{bmatrix}, \qquad [I_{AI}] = \begin{bmatrix} P & 0 & 0 \\ 0 & Q & 0 \\ 0 & 0 & R \end{bmatrix} \qquad (15)$$

The dynamic equations of motion are found by substituting all forces and moments into Eqs. (4) and (5), resulting in the matrix solution in Eqs. (16–18)

$$\begin{bmatrix} m[I] + [I_{AM}] & -[I_{AM}][S^B_{cg,M}] \\ [S^B_{cg,M}][I_{AM}] & [I_T] + [I_{AI}] - [S^B_{cg,M}][I_{AM}][S^B_{cg,M}] \end{bmatrix} \begin{Bmatrix} \dot{u} \\ \dot{v} \\ \dot{w} \\ \cdots \\ \dot{p} \\ \dot{q} \\ \dot{r} \end{Bmatrix}$$

$$= \begin{bmatrix} B_1 \\ \cdots \\ B_2 \end{bmatrix} \qquad (16)$$

$$B_1 = -m[S^B_\omega] \begin{Bmatrix} u \\ v \\ w \end{Bmatrix} + \begin{Bmatrix} X_W \\ Y_W \\ Z_W \end{Bmatrix} + \begin{Bmatrix} X_{A,P} \\ Y_{A,P} \\ Z_{A,P} \end{Bmatrix} + \sum_i \begin{Bmatrix} X_{A,i} \\ Y_{A,i} \\ Z_{A,i} \end{Bmatrix} \qquad (17)$$

$$B_2 = -[S^B_\omega][I_T] \begin{Bmatrix} p \\ q \\ r \end{Bmatrix} + [S^B_{cg,P}] \begin{Bmatrix} X_{A,P} \\ Y_{A,P} \\ Z_{A,P} \end{Bmatrix} + \sum_i [S^B_{cg,i}] \begin{Bmatrix} X_{A,i} \\ Y_{A,i} \\ Z_{A,i} \end{Bmatrix} \qquad (18)$$

Equation (16) represents a set of coupled, nonlinear differential equations. The matrix on the left hand side of Eq. (16) is a function of the mass and geometry properties of the parafoil. The geometry of the parafoil is assumed to be fixed, so this matrix is constant and only needs to be inverted once at the beginning of the simulation. With specified initial conditions, the states can be numerically integrated forward in time.

## III. In-Flight System Identification

### A. Overview of Process

With current autonomous parafoil and payload systems, typically only lateral control is used to guide the parafoil to the target [1–8]. This reduces the parafoil trajectory planning problem to generating a desired trajectory in the horizontal plane in the form of heading commands, which in turn reduces the control problem to tracking a desired heading with a single lateral control input. In the presence of wind, it is normally desirable to generate the trajectory in a wind-relative reference frame so that the commanded heading to be tracked is actually the wind-relative azimuth angle $\chi_0$. This quantity corresponds to the Euler yaw angle $\psi$, when the sideslip is zero, as shown in Fig. 2. This means that the autonomous control law is designed based on an estimate of the wind-relative azimuthal rate dynamics. Determination of these dynamics relies on the solution of the vector diagram in Fig. 2. The forward airspeed component $V_0$ is assumed to remain constant during each flight and will be identified in-flight. If a heading measurement is available, the sideslip is neglected ($\psi \approx \chi_0$), so that the vector diagram in Fig. 2 is fully defined. Without a heading measurement, the wind-relative velocity vector can be determined over a series of measurements by assuming that the wind vector changes slowly, similar to Jann [5], as well as Carter et al. [6].

The overall flight procedure requires four key flight segments: 1) zero control input, 2) track a heading command, 3) complete a circle in one direction, and 4) turn briefly in the other direction. The
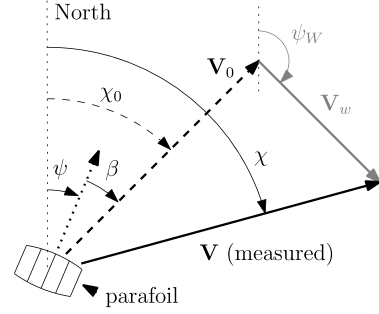


Fig. 2 Decomposing measured velocity vector (top view).

flight segments can be executed separately at any time during the flight and in any order. After the flight segments have been completed, the in-flight system identification process is executed as follows: 1) estimate the forward airspeed and initialize the wind estimate, 2) generate a stream of wind-relative azimuthal rate data for key flight segments, 3) derive a mapping of control input to steady-state turn rate from the azimuthal rate data, and 4) identify the turn rate dynamics from azimuthal rate data.

The first two flight segments correspond to the typical initial segments of a guided parafoil drop (allow the system to reach an initial equilibrium then point at some waypoint), and they are used to estimate the control bias. The circling segment is used to estimate the forward airspeed, and the circling segment combined with the last segment constitutes a brake doublet, which is used to estimate the turn rate dynamics.

### B. Estimating Forward Airspeed

The circling segment of the fight procedure is flown until it is apparent from the ground track azimuth measured with GPS that at least one complete circle has been flown. The ground track azimuth data is then processed to precisely estimate the beginning and end of a single complete circle. The instants marking the beginning and end of the complete circle are denoted as $i$ and $f$, respectively. Equation (19) is then used to estimate the forward airspeed, where the mean value is computed over the entire set of measurements for the complete circle ($i \leq k \leq j$). The drift in the system position over the complete circle is also used to initialize the wind estimates

$$V_0 = \text{mean} \left[ \sqrt{ \left( \dot{x}_k - \frac{x_f - x_i}{t_f - t_i} \right)^2 + \left( \dot{y}_k - \frac{y_f - y_i}{t_f - t_i} \right)^2 } \right] \qquad (19)$$

### C. State Estimation

The goal of the state estimation process is to produce an estimate of the wind and a stream of wind-relative azimuthal rate data $\dot{\chi}_0(t)$, from which the system dynamics can be identified. The observer is an extended Kalman filter [17]. The system state vector $\mathbf{x}_k$ and measurement vector $\mathbf{z}_k$ are considered to be nonlinear functions

$$\begin{cases} \mathbf{x}_{k+1} = \mathbf{f}_k(\mathbf{x}_k) + [N_k(\mathbf{x}_k)]\mathbf{n}_k \\ \mathbf{z}_k = \mathbf{g}_k(\mathbf{x}_k) + \mathbf{w}_k \end{cases} \qquad (20)$$

where $\mathbf{n}_k$ is the process noise vector, and $\mathbf{w}_k$ is the measurement noise vector, both of which are assumed to be zero-mean Gaussian white noise sequences.

The wind vector and the aerodynamic velocity vector are defined as states in the observer $\mathbf{x}_k$, so the state update equations $\mathbf{f}_k(\mathbf{x}_k)$ are defined by the vector geometry that relates these states to the measured ground track velocity vector (Fig. 2). These equations assume that the wind vector, airspeed, and wind-relative azimuthal rate are all constants that are perturbed by a process noise vector $\mathbf{n}_k$ consisting of independent perturbations to the north and south wind components, airspeed, and azimuthal rate ($\delta V_{wx}, \delta V_{wy}, \delta V_0$, and $\delta \dot{\chi}_0$, respectively). The observer state update equations are given in Eq. (21)

$$\mathbf{x}_k = \begin{pmatrix} x_k \\ y_k \\ \dot{x}_k \\ \dot{y}_k \\ V_{wxk} \\ V_{wyk} \\ \chi_{0k} \\ \dot{\chi}_{0k} \\ \mathbf{z}_{bk} \end{pmatrix}, \mathbf{f}_k(\mathbf{x}_k) = \begin{pmatrix} x_k + \dot{x}_k \Delta t \\ y_k + \dot{y}_k \Delta t \\ V_0 \cos(\chi_{0k}) + V_{wxk} \\ V_0 \sin(\chi_{0k}) + V_{wyk} \\ V_{wxk} \\ V_{wyk} \\ \chi_{0k} + \dot{\chi}_{0k} \Delta t \\ \dot{\chi}_{0k} \\ \mathbf{z}_{bk} \end{pmatrix}, [N_k(\mathbf{x}_k)]\mathbf{n}_k$$

$$= \begin{pmatrix} 0 \\ 0 \\ \cos(\chi_{0k})\delta V_0 \\ \sin(\chi_{0k})\delta V_0 \\ \delta V_{wx} \\ \delta V_{wy} \\ 0 \\ \delta \dot{\chi}_0 \\ \delta \mathbf{x}_b \end{pmatrix} \quad (21)$$

There are two measurement cases considered, GPS only and GPS with a heading measurement. The measurement vector from GPS ($\mathbf{z}_k$) consists of north and east position and north and east velocity components, and the heading measurement is assumed to represent the wind-relative azimuth (zero sideslip assumption). To make the process more robust to measurement error, biases in the velocity vector and heading angle measurements are also estimated by appending them to the state vector [$\mathbf{z}_b$ in Eq. (21), where $\mathbf{z}_b = \{z_{b\dot{x}}, z_{b\dot{y}}\}^T$ for GPS only and $\mathbf{z}_b = \{z_{b\dot{x}}, z_{b\dot{y}}, z_{b\psi}\}^T$ for GPS with a heading measurement]. The measurement vector is shown in Eq. (22); the last entry $z_\psi$ is not present for the GPS only case

$$\mathbf{z}_k = \begin{pmatrix} z_{xk} \\ z_{yk} \\ z_{\dot{x}k} \\ z_{\dot{y}k} \\ z_{\psi k} \end{pmatrix}, \mathbf{g}_k(\mathbf{x}_k) = \begin{pmatrix} x_k \\ y_k \\ \dot{x}_k + z_{b\dot{x}k} \\ \dot{y}_k + z_{b\dot{y}k} \\ \chi_{0k+z_{b\psi k}} \end{pmatrix}' = \mathbf{w}_k = \begin{pmatrix} w_x \\ w_y \\ w_{\dot{x}} \\ w_{\dot{y}} \\ w_\psi \end{pmatrix} \quad (22)$$

### D. Steady-State Turn Rate

The mapping of control input to steady-state turn rate is performed separately from the estimation of the transient characteristics of the lateral dynamics. The idea is that there is a deterministic mapping from each left and right brake position to steady-state turn rate, and while this mapping is not generally linear [10,18] the dynamics that describe how the turn rate reaches the given steady-state value may be approximated as linear. The current work assumes that the control



**Fig. 3 Mapping left and right brake to steady-state turn rate.**

deflection is limited to a region where the steady-state turn rate is approximately proportional to control deflection, so the control to turn rate mapping need only account for control bias and asymmetric control sensitivity. Four points of steady-state turn rate data corresponding to the four key flight segments are computed from the azimuthal rate estimates produced by the observer. These four points are used to generate the linear mapping from control input to steady-state turn rate as shown in Fig. 3.

### E. Turn Rate Dynamics

The open-loop wind-relative azimuthal rate dynamics are approximated as a first order filter of the steady-state turn rate

$$\dot{\chi}_{0,k+1} = \dot{\chi}_{0,k} + (\dot{\chi}_{0,ss} - \dot{\chi}_{0,k})/\tau \quad (23)$$

This leaves only the azimuthal rate time constant $\tau$ to be estimated from the data stream produced by the observer. The assumption that the turning dynamics can be approximated as a first order system was made based on the authors' experience flight testing small parafoils. Nonlinear simulation results for the example systems also appear to be approximately first order, and there is at least one example in the literature where the turning dynamics from flight-test data of a medium sized (250 lb) system appeared to be reasonably approximated as first order [19]. However, second-order turning dynamics have been observed for some systems in-flight test [3,20]. The approach described in the present work can be applied to these systems by modifying Eq. (23) to account for second-order dynamics so that two dynamic parameters (e.g., natural frequency and damping ratio) would need to be identified rather than one. Another possibility is that the rate limit on the brake deflection may be such that the lateral dynamics are never excited, so that the system is always flying at the steady-state turn rate [18,21]. In this case, only the mapping of control input to steady-state turn rate would need to be identified.

The time constant is determined from the estimated azimuthal rate data by a Gauss–Newton optimizer to minimize the error between the observed azimuthal rate and the azimuthal rate predicted with Eq. (23). The optimization process was found to be robust in the presence of large disturbances during the system identification maneuvers. Also, while the use of an optimizer in system identification is normally one of the more computationally intensive approaches, the current problem can be solved very quickly because there is only one parameter, the objective function is quickly determined by propagating Eq. (23), and the problem is well conditioned so that it normally converges in less than five iterations.

## IV. Simulation Parameters

### A. Example Parafoil and Payload System Parameters

To investigate the characteristics of the in-flight estimation procedure, a large and a small parafoil system were considered (Fig. 4). These two systems span the entire range of autonomous airdrop systems. The physical and aerodynamic parameters for both parafoils can be found in Tables 1 and 2, while Fig. 5 defines some of the geometry parameters used in the tables. Parameters for both parafoils were chosen to match flight-test data [4,14]. The values for these parameters represent a nominal model of each vehicle. A significant amount of variability in the flight dynamics from flight-to-flight was observed in the flight-test data. Estimates for these levels of uncertainty form the basis for the Monte Carlo simulations discussed below.

The canopy brakes are assumed to extend across both outer panels for the Megafly (panels 1, 2, 4, and 5 in Fig. 1) and across only the outermost panels for the microparafoil. The control sensitivities ($C_{L\delta,i}$ and $C_{D\delta,i}$) are normalized so that a control input of 1 produces a 5 deg/s turn rate for the Megafly and a 20 deg/s turn rate for the microparafoil. The Megafly turn rate limit was chosen based on the turn rate limit specified in [4]. The microparafoil turn rate limit was chosen to avoid a nonlinear spiraling behavior at high brake deflections. Rate limits are imposed on the brake deflections so that it
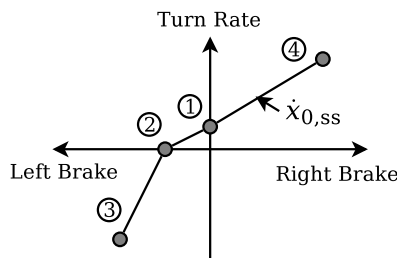
a) 30k Megafly (Ref. [17])                                    b) Micro Parafoil

Fig. 4    Megafly and microparafoil systems.

takes 5 s to reach full brake deflection for the Megafly, and 1 s to reach full brake deflection for the microparafoil.

### B.    Simulated Measurement Parameters

Measurements from a GPS unit are assumed to be available for all flights, and a heading measurement is added for some flights. GPS sensor errors are modeled as exponentially correlated Gaussian noise and heading sensor error is modeled as Gaussian white noise [22,23]. In addition, each sensor is given a bias that is constant over each flight and follows a Gaussian distribution over a series of flights. The form of the measurement signals is given in Eq. (24), where $y_k$ is the actual value, $z_k$ is the measured value, $n_k$ is the measurement noise, and $\delta_B$ is the measurement bias. Sensor parameters were selected to represent low-cost, commercially available sensors. The position measurements are given a standard deviation of 2 m for the noise, a standard deviation of 1 m for the bias, and a time constant of 20 s. The velocity measurements are given a standard deviation of 0.2 m/s the noise, a standard deviation of 0.1 m/s for the bias, and a time constant of 1 s. The heading measurement noise is given a standard deviation of 2 deg and the bias is given a standard deviation of 10 deg. The sampling interval $\Delta t$ is set for a 4 Hz update rate for all measurements

$$
\begin{cases}
z_k = y_k + n_k + \delta_B \\
n_k = e^{-\Delta t/\tau_e} n_{k-1} + \xi_k \sqrt{1 - e^{-2\Delta t/\tau_e}} \\
\xi_k \sim N(0, \sigma_N) \\
\delta_B \sim N(0, \sigma_B)
\end{cases}
\tag{24}
$$

The observer requires estimates of the variances of the process noise and measurement noise components. The measurement noise variances are set to the actual values for each measurement. For the process noise, standard deviations of 1 m/s for the aerodynamic velocity perturbation $\delta V_0$ and 0.001 rad/s for the azimuthal rate perturbation $\delta \dot{\chi}_0$ are assumed. If only GPS measurements are available, the wind perturbations ($\delta V_{wx}, \delta V_{wy}$) are assumed to have standard deviations of 0.0001 m/s, but if a heading measurement is added, this value is increased to 0.01 m/s. The standard deviations for the GPS velocity measurement biases ($\delta_B \dot{x}, \delta_B \dot{y}$) are set to $1E - 5$ m/s, and the standard deviation for the heading measurement bias is set to $1E - 6$ rad.

### C.    Wind Model

A simplified Dryden turbulence model [24] is used to simulate atmospheric winds with the wind magnitude and direction represented as exponentially correlated Gaussian random variables. The standard deviation of the wind magnitude is assumed to be 10% of the mean wind magnitude, and the standard deviation of the wind direction is assumed to be 10 deg. The time constants for the wind magnitude and direction were both chosen to be 10 s. Vertical winds are not simulated.

Table 1    Megafly and microparafoil physical parameters

| Parameter | Megafly | Microparafoil | Units |
|---|---|---|---|
| $d$ | 30 | 1.2 | m |
| $\Lambda$ | 120 | 70 | deg |
| $b$ | 51.8 | 1.37 | m |
| $c$ | 16.3 | 0.64 | m |
| $S_C$ | 840 | 0.93 | m$^2$ |
| $S_P$ | 9.0 | 0.033 | m$^2$ |
| Total mass | 13,605 | 2.37 | kg |
| $I_{XX}$ | 361,650 | 0.42 | kg m$^2$ |
| $I_{YY}$ | 328,200 | 0.40 | kg m$^2$ |
| $I_{ZZ}$ | 131,400 | 0.05 | kg m$^2$ |
| $I_{XZ}$ | $-2,283$ | 0.03 | kg m$^2$ |
| $A$ | 293 | 0.01 | kg |
| $B$ | 3,133 | 0.05 | kg |
| $C$ | 9,858 | 0.40 | kg |
| $P$ | 78,960 | 0.008 | kg m$^2$ |
| $Q$ | 102,560 | 0.007 | kg m$^2$ |
| $R$ | 84,590 | 0.002 | kg m$^2$ |

Table 2    Megafly and microparafoil aerodynamic parameters

| Coefficient | Megafly | Microparafoil |
|---|---|---|
| $C_{L0,i}$ | 0.45 | 0.30 |
| $C_{L\alpha,i}$ | 2.2 | 0.723 |
| $C_{L\alpha3,i}$ | $-1.0$ | $-0.35$ |
| $C_{L\delta,i}$ | 0.125 | 0.0065 |
| $C_{D0,i}$ | 0.15 | 0.12 |
| $C_{D\alpha2,i}$ | 1.5 | 0.90 |
| $C_{D\delta,i}$ | 0.125 | 0.010 |
| $C_{D,P}$ | 0.8 | 0.3 |

Fig. 5   Geometry parameters.

model of the azimuthal rate dynamics that was tuned to match the nominal simulation model. This represents the fixed model that would normally be derived from an initial set of flight tests and loaded on to the flight computer before each drop. The other two trajectories were generated using azimuthal rate models derived with the in-flight system identification procedure with and without the specified sensor errors.

Figure 6 demonstrates the tradeoff with in-flight identification. The in-flight identification process uses data that is corrupted by sensor noise and wind disturbances, so a perfect realization of the system dynamics cannot be achieved. If there is very little variability in the parafoil dynamics, then a precomputed model of the nominal system will always be a good representation, but if the level of variability is high enough relative to the sensor errors and wind disturbances, then a better representation will be obtained with a dynamic model identified in-flight. A challenge for autonomous airdrop system designers is to understand when it is preferable to perform system identification in-flight and when a precomputed model should be used.

## V.   Example Trajectory Predictions

Figure 6 shows 10 s of a simulated trajectory of the microparafoil with a 50% step left brake input. Figure 6a represents the nominal simulation model, and Fig. 6b represents a modified model with a 15% right control bias and the left brake effectiveness reduced by 15%. The fixed linear model trajectory was generated from a linear

## VI.   Example Wind and Wind-Relative Dynamics Estimation

The turn rate dynamics during a 50% left brake step input for the Megafly and microparafoil simulation models are shown in Fig. 7. There is no wind in these cases, so the azimuthal rate corresponds to the wind-relative azimuthal rate. The azimuthal rate response of the Megafly and microparafoil simulation models both appear to be
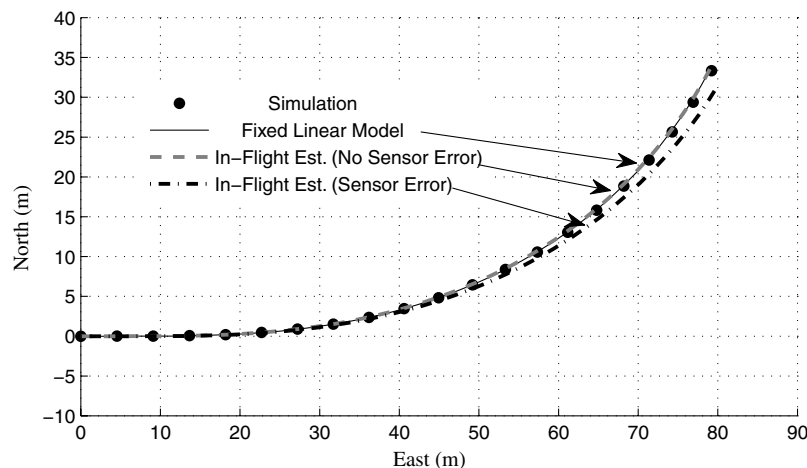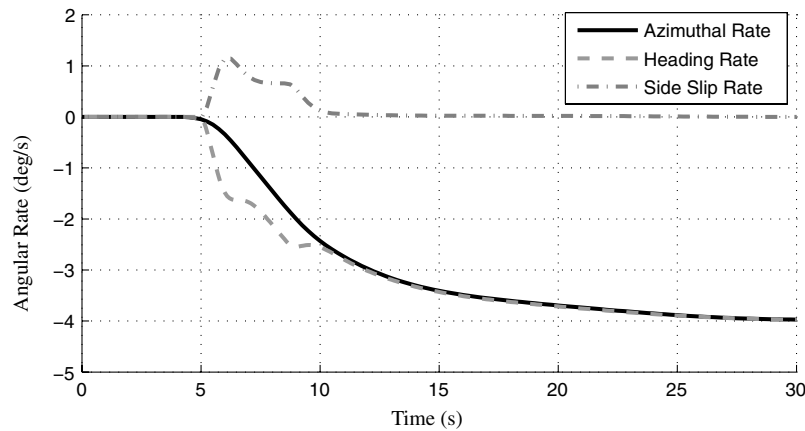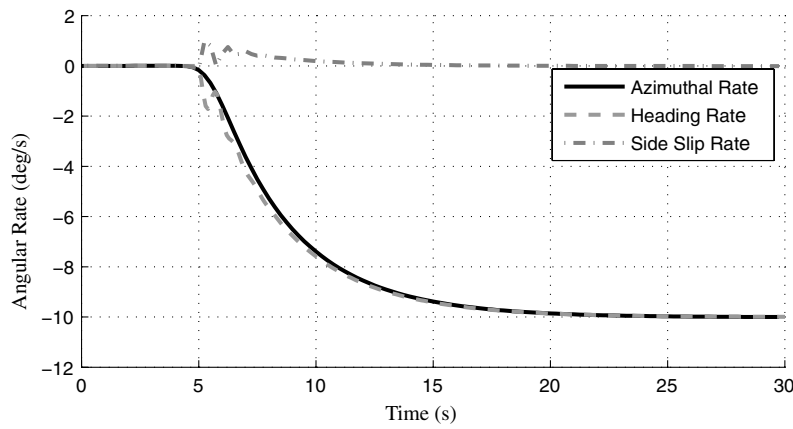


a) Nominal simulation model
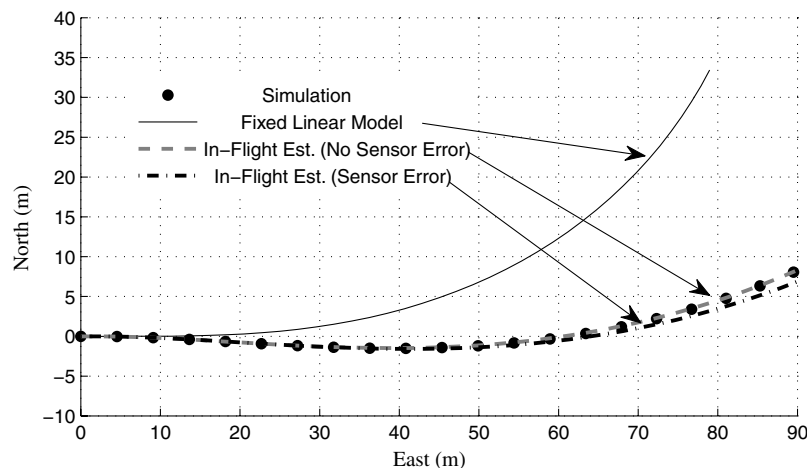


b) Modified simulation model

Fig. 6   Microparafoil example trajectories with a) nominal simulation model, and b) with 15% right control bias and left brake effectiveness reduced by 15%.

a) Megafly



b) Microparafoil

Fig. 7   Megafly (part a) and microparafoil (part b) azimuthal and heading rate response.

approximately first order. However, the simulation models have very different sideslip dynamics. The microparafoil turns with very little sideslip, but the tendency of the Megafly to turn with a significant sideslip causes the heading rate to initially lead the azimuthal rate.

Wind-relative azimuthal rate estimates obtained from the Kalman filter observer during a left brake step input using the Megafly and microparafoil simulation models are shown in Fig. 8. In both cases, the mean wind magnitude is 10 m/s. The mean squared error for the microparafoil is reduced by 37% with the addition of the heading sensor, but the error for the Megafly is only reduced by 15% with the addition of the heading sensor. It is expected that the benefit from the heading sensor is reduced for the Megafly because of the increased amount of sideslip compared with the microparafoil, as shown in Fig. 7. A second factor contributing to the large reduction in estimation error for the microparafoil is that the wind-relative azimuthal rate estimation with GPS is very sensitive to the wind estimate for the microparafoil because the forward flight speed of the microparafoil ($\sim$9 m/s) is close to the wind speed in this case, while the forward speed of the Megafly ($\sim$20 m/s) is about double the wind speed.

The associated wind estimates for these simulations are shown in Figs. 9 and 10. Note that with GPS only, the wind estimate is a slowly varying average magnitude and direction, while the addition of the heading sensor provides a significant improvement in the wind estimation for both the Megafly and the microparafoil.

## VII.   Monte Carlo Simulation Results

### A.   Results for Assumed Levels of Model Uncertainty, Sensor Noise, and Wind

A Monte Carlo simulation was run to assess the benefits of performing the system identification in-flight compared with using a fixed model of the nominal system. Levels of model uncertainty were

selected based on flight-test experience. While every parameter listed in Tables 1 and 2 has an associated uncertainty, the same overall effects are achieved by varying a few key parameters. The wind magnitude was set to vary from zero to the expected airspeed of each system to cover the entire operational envelope. All of the random variables in the Monte Carlo simulation were uniformly distributed with the following ranges: $\pm$15% asymmetric control bias, $\pm$25% left and right control sensitivities, $\pm$25% payload weight, and $\pm$5% $C_{L0}$ and $C_{D0}$ for the entire canopy. The mean wind speed was varied uniformly from 0–10 m/s for the microparafoil and from 0–20 m/s for the Megafly. One hundred cases were run for each parafoil system. All of the errors in the quantities estimated in-flight from the simulated measurement data are compared with the errors that would results from the use of a fixed model that would normally be derived from an initial set of flight tests and loaded on to the flight computer before each drop. These fixed model errors also represent the perturbations in each estimated quantity that are induced by the assumed levels of model uncertainty.

Figures 11 and 12 show the error distributions for the estimated time constant of the azimuthal rate dynamics for the Megafly and microparafoil. Estimates using GPS only and using GPS in conjunction with a heading measurement are shown. The time constant error is the difference between the estimated time constant and an optimal time constant obtained by fitting the actual wind-relative azimuthal rate data from the nonlinear simulation model. The values for the time constant error are on the order of 20%. Figure 13 demonstrates the effect of a 20% change in time constant on the turn rate response to a step input. Comparison of this figure to the example azimuthal rate estimates in Fig. 8, provides some qualitative insight in the difficulties of in-flight estimation of dynamic parameters with typical levels of sensor noise and turbulence. Figures 11 and 12 show that the standard deviation of the time constant estimation error is reduced by the addition of the heading measurement for both parafoils, but the
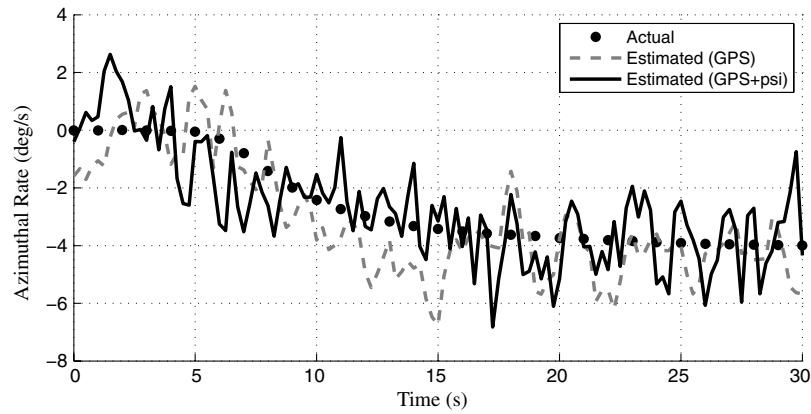
a) Megafly
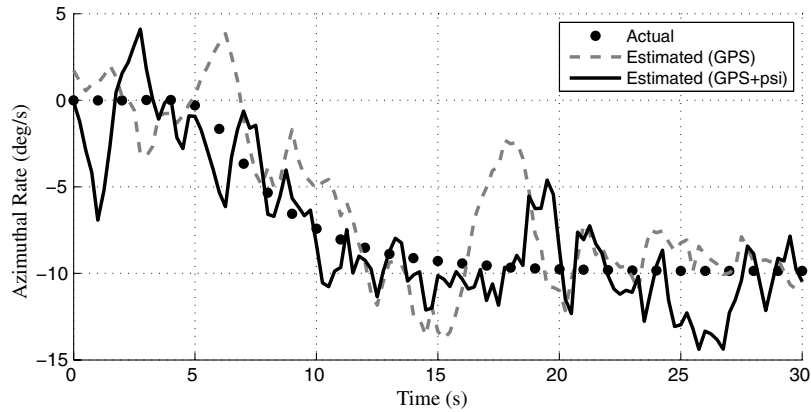


b) Microparafoil

Fig. 8   Megafly (part a) and microparafoil (part b) example wind-relative azimuthal rate estimation.

effect on the mean of the time constant error is different. There is a lag associated with the filtered azimuthal rate estimate, so it is expected that the estimated time constant would be generally higher than the optimal value, resulting in a positive shift to the mean error. The dramatic shift in the mean time constant error for the Megafly can be explained by the sideslip behavior shown in Fig. 7. The tendency of the heading rate to initially lead the azimuthal rate for the Megafly causes the wind-relative azimuthal rate estimate to appear to respond artificially quickly to control input, which results in lower estimates

for the time constant when the heading sensor is added. The microparafoil turns with very little sideslip, so no shift in the time constant error is observed when the heading sensor is added.

Figures 14 and 15 show the error distributions for the in-flight control bias and airspeed estimations. The techniques for estimating the control bias and airspeed do not depend on the heading measurement, so the results are the same for both sensor cases. Note that the airspeed estimation error is skewed for the Megafly. This is because the airspeed is estimated during a turn, and the Megafly
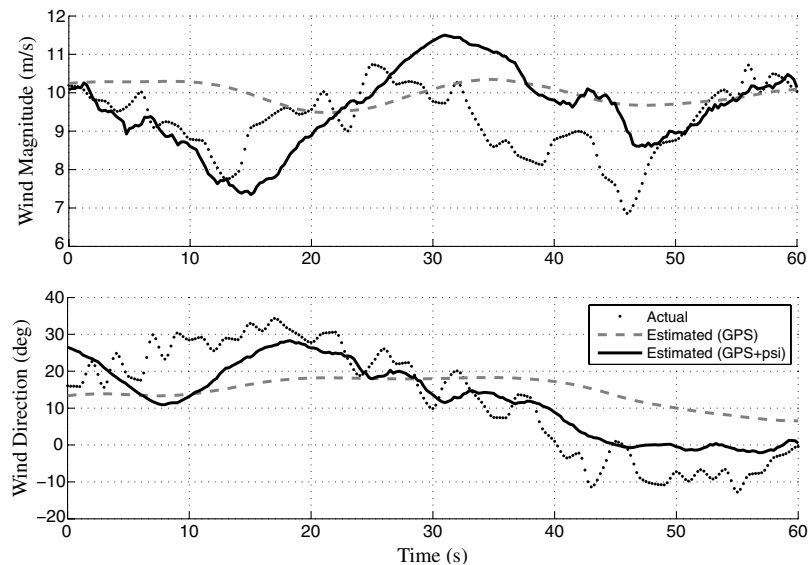


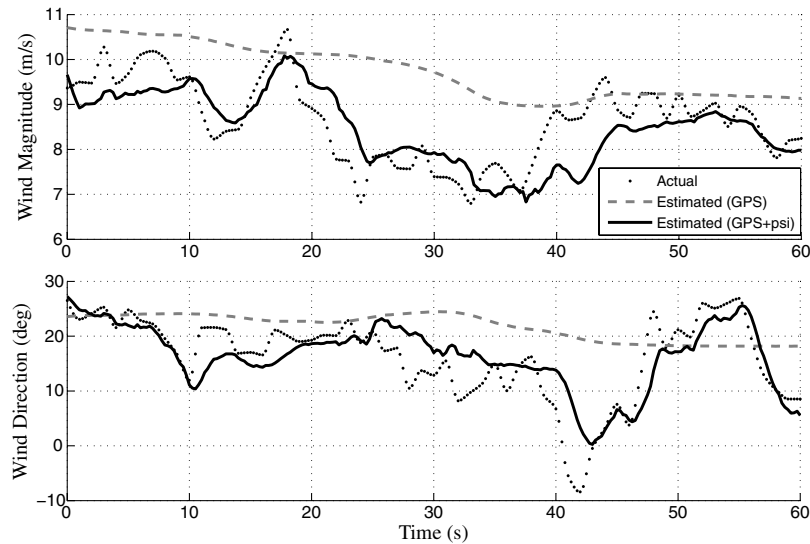Fig. 9   Megafly example wind estimation.
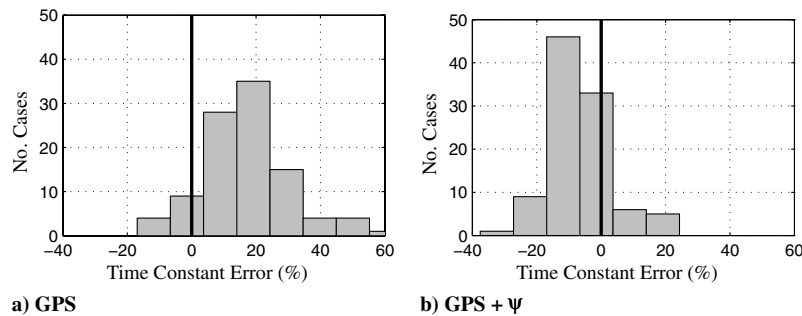
Fig. 10    Microparafoil example wind estimation.



a) GPS                                    b) GPS + Ψ

Fig. 11    Monte Carlo results: Megafly time constant error.



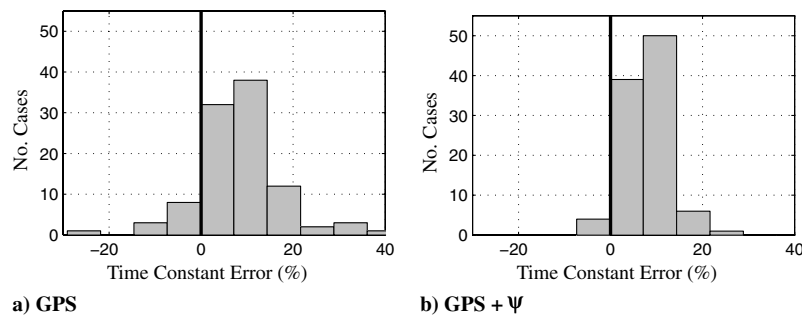a) GPS                                    b) GPS + Ψ

Fig. 12    Monte Carlo results: microparafoil time constant error.

system exhibits a tendency to slow down while turning due to the large span of the canopy brakes. The microparafoil showed no such tendency.

Figure 16 shows the steady-state turn rate response estimation error. From each Monte Carlo run, an estimation of the steady-state turn rate vs control input is obtained. By subtracting the actual steady-state turn rate vs control input produced by the simulation model for that particular run, a discrete value of turn rate error at each control input is obtained. Compiling the results for all of the Monte Carlo runs, these discrete values become distributions of turn rate estimation error at each control input. By excluding the upper and lower 5% of these distributions, upper and lower bounds enclosing 90% of the cases at each control input are determined. These bounds are plotted in Fig. 16. The average widths of each of these 90% turn rate error bounds are reported in the last row of Table 3 as mean 90% turn rate error bound. The results show that the addition of a heading sensor provides a slight improvement in turn rate estimation, but
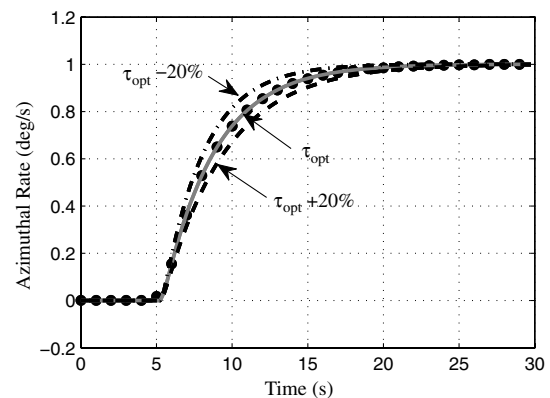


Fig. 13    Microparafoil step response demonstrating time constant errors.
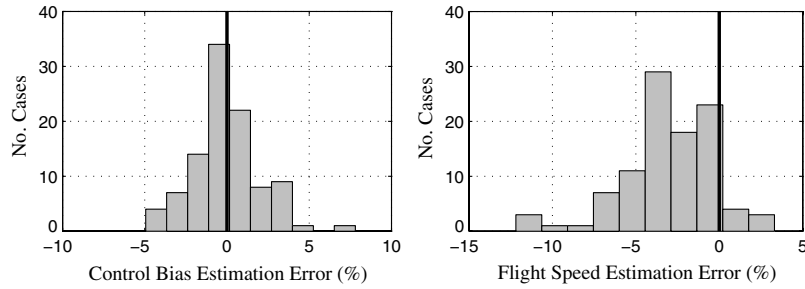
**Fig. 14    Monte Carlo results: Megafly control bias and airspeed estimation error.**
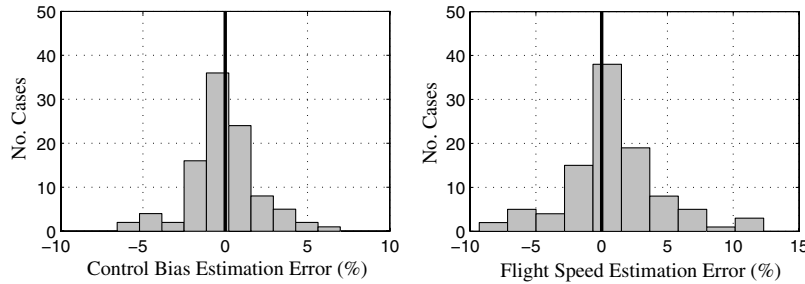


**Fig. 15    Monte Carlo results: microparafoil control bias and airspeed estimation error.**

overall the estimation of steady-state turn rate is robust for both sensor cases.

All of the results from the Monte Carlo simulation are summarized in Table 3. It is clearly beneficial to estimate all of the steady-state characteristics of the system (airspeed, control bias, and turn rate) in-flight. In-flight estimation of the airspeed for the microparafoil significantly reduces the airspeed error, and for the Megafly the

airspeed error is cut in half. Control bias error is reduced by more than a factor of 3 for both parafoils. Turn rate error is reduced by a factor of 6 for the microparafoil, and by more than a factor of 4 for the Megafly. The estimation of the azimuthal time constant in-flight with a heading measurement produces similar standard deviations to the fixed model, though there is a significant increase in the mean time constant error. For the case where only GPS measurements are used,
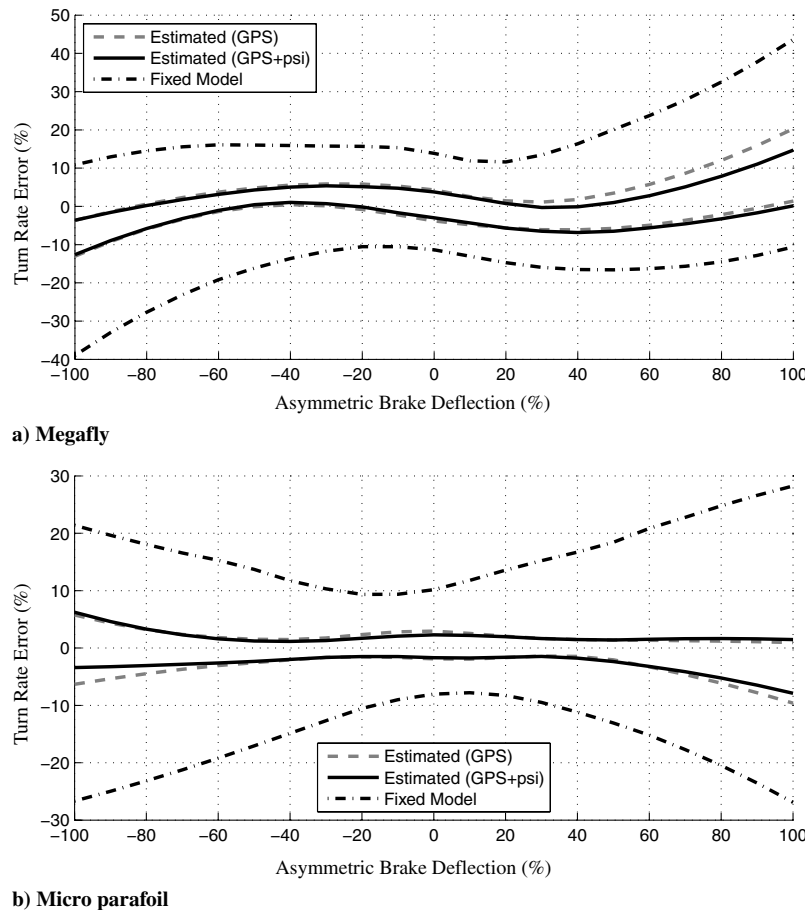


**a) Megafly**



**b) Micro parafoil**

**Fig. 16    Monte Carlo results: Megafly (part a) and microparafoil (part b) steady-state turn rate estimation error.**

Table 3 Monte Carlo simulation results[a]

| Error description | Microparafoil | | | Megafly | | |
|---|---|---|---|---|---|---|
| | Fixed model | GPS | GPS + $\psi$ | Fixed model | GPS | GPS + $\psi$ |
| Mean flight-test speed | −0.2 | 1.1 | | −1.9 | −3.1 | |
| Standard deviation flight-test speed | 6.3 | 3.8 | | 7.3 | 2.9 | |
| Mean control bias | 0.0 | 0.0 | | 0.0 | 0.0 | |
| Standard deviation control bias | 6.8 | 2.1 | | 7.1 | 2.1 | |
| Mean time constant | −2.1 | 8.2 | 8.2 | 4.1 | 17.3 | −6.3 |
| Standard deviation time constant | 5.6 | 9.5 | 5.0 | 6.5 | 13.9 | 9.8 |
| Mean 90% turn rate error bound | 33.1 | 5.7 | 5.0 | 36.4 | 8.8 | 7.3 |

[a]Errors are percentages.

in-flight estimation of the time constant results in larger errors than the use of a fixed model. This indicates that in-flight estimation of the time constant is not generally beneficial when only GPS measurements are available.

## B. Sensitivity to Levels of Model Uncertainty, Sensor Noise, and Wind

An additional set of Monte Carlo simulations was run to investigate the sensitivity of the results to changes in the assumed levels of sensor error, model uncertainty, and wind levels. The model uncertainty levels used in the first simulation were scaled from zero



Fig. 17   Explanation of in-flight identification vs fixed model boundaries.

(perfect knowledge of the system) to 1.5 times the given ranges. The standard deviations for all of the sensor errors were scaled from zero (perfect sensors) to 2 times the given levels. The microparafoil simulation model was used for these runs. Cases were run with no wind and with constant mean wind magnitudes of 5 m/s (∼half system airspeed) and 10 m/s (∼equal to system airspeed). From the results, the boundaries where the in-flight system identification and the fixed model produce the same errors in the steady-state and transient turn response were calculated as a function of the model uncertainty and sensor error levels at the three different wind levels. Figure 17 explains how these boundaries are plotted. With model uncertainty on the $y$ axis and sensor error on the $x$ axis, the region above and to the left of the boundaries represents the space where the model uncertainty is large enough and the sensor data is good enough that it is better to perform the system identification in-flight as opposed to using a fixed model of the flight dynamics. The actual results are shown in Figs. 18 and 19.

Figure 18 shows that if there is any flight-to-flight variation in the system at all, then it is better to estimate the steady-state characteristics of the system in-flight. It also shows that with the addition of a heading measurement, the in-flight estimation of the steady-state characteristics is made more robust to large levels of sensor noise. Figure 19 shows that when only GPS measurements are available it is difficult to obtain a good estimation of the transient response with moderate to high wind levels. The boundary for the 10 m/s wind case lies off the chart because it is better to use a fixed model over the entire range of sensor error and model uncertainty considered. For the results with the heading sensor included, the boundaries run through the assumed levels of model uncertainty and sensor errors, implying that it makes little difference if the time constant is estimated in-flight or if a precomputed time constant is used.
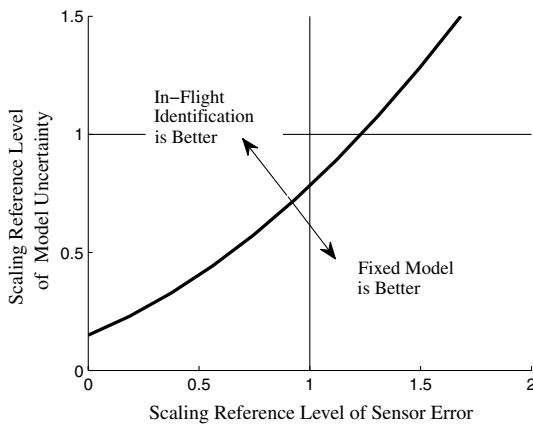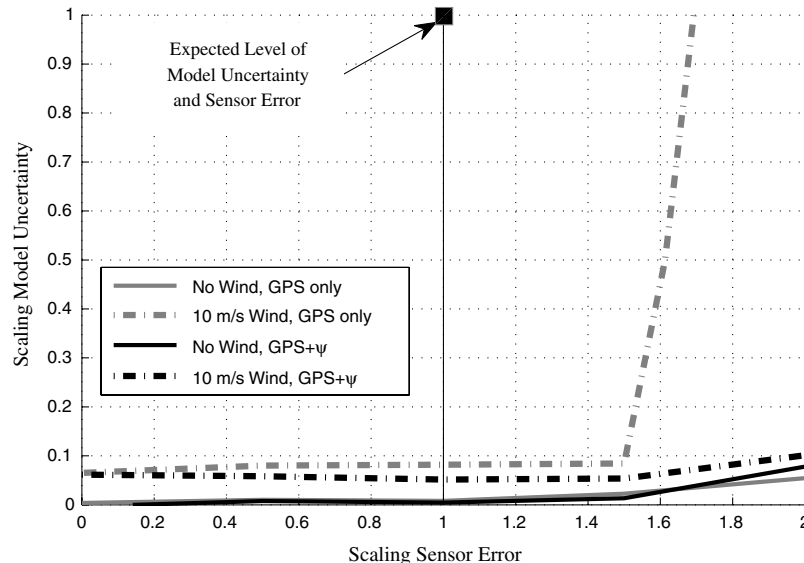


Fig. 18   In-flight identification vs fixed model boundaries for steady-state response.
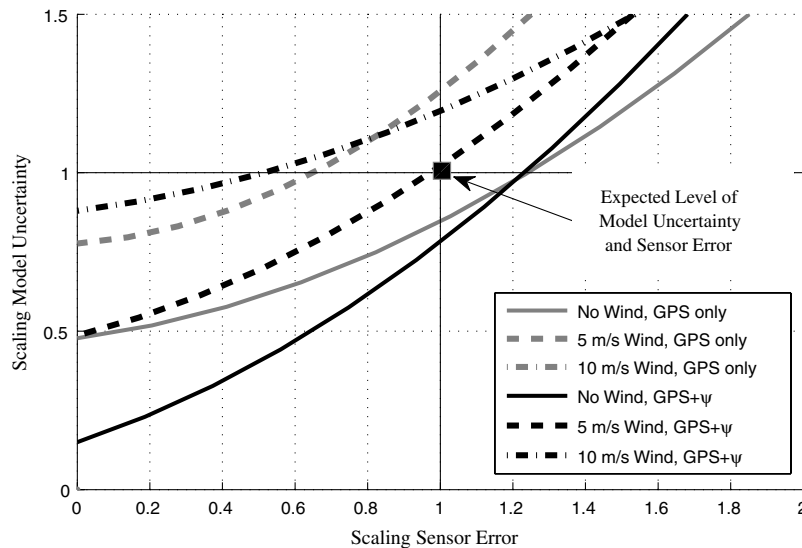
**Fig. 19   In-flight identification vs fixed model boundaries for transient response.**

System identification relies on state estimates that are degraded by atmospheric turbulence and sensor errors. The traditional scenario when system identification is performed on the ground takes advantage of the ability to estimate parameters over multiple maneuvers and multiple flights so that the effects of sensor errors and turbulence are averaged out. The results presented here show that it is always beneficial to estimate steady-state quantities in-flight with reasonable levels of model uncertainty, sensor noise, and wind because the estimation is performed by averaging over a series of measurements. On the other hand, transient characteristics estimated in-flight over the small windows of data during maneuvers are much more sensitive to sensor noise and turbulence, and the results show that it is not always beneficial to estimate these transient characteristics in-flight. In other words, for transient characteristics, the degradation in the quality of in-flight estimates from sensor noise and turbulence is comparable to the degradation in the quality of fixed estimates from model uncertainty.

## VIII.   Conclusions

Dynamic characteristics of airdrop systems vary substantially from drop to drop, more than most other air vehicles. This paper addresses the question of whether it is more appropriate to use precomputed dynamic characteristics of an airdrop system inside an autonomous control law or whether it is better to estimate these characteristics in-flight. A simulation study was performed using a 6 degrees of freedom nonlinear parafoil and payload simulation with an associated estimation algorithm. Simulation results with typical levels of sensor errors and model uncertainty demonstrate that the system identification procedure provides significantly better estimates of the system dynamics than a precomputed, nominal model. Errors in predicted steady-state turn rate were reduced by a factor of more than 4 for the Megafly and by a factor of 6 for the microparafoil. It was found by varying the assumed levels of sensor errors, model uncertainty, and wind that the in-flight identification of the steady-state characteristics of airspeed, control bias, and turn rate behavior is always beneficial. This is because steady-state quantities are estimated by averaging over a series of measurements so that the detrimental effects of sensor noise and turbulence are reduced. In contrast, the in-flight identification of the azimuthal rate time constant was found to produce results that were comparable to a fixed, nominal model if a heading measurement is available, and the in-flight identification results when using only GPS were not as good as the fixed model for moderate to high wind levels. This result stems from the more general conclusion that with typical levels of sensor noise and atmospheric turbulence it is very difficult to obtain reliable azimuthal rate estimates for an airdrop system during a maneuver without a heading estimate. This suggests that the success of any

adaptive control scheme for airdrop systems is critically dependent on the incorporation of high quality heading estimates.

## References

[1] Calise, A., and Preston, D., "Design of a Stability Augmentation System for Airdrop of Autonomous Guided Parafoils," AIAA Paper 2006-6776, May 2006.

[2] Calise, A., and Preston, D., "Swarming/Flocking and Collision Avoidance for Mass Airdrop of Autonomous Guided Parafoils," *Journal of Guidance, Control, and Dynamics*, Vol. 31, No. 4, 2008, pp. 1123–1132.
doi:10.2514/1.28586

[3] Carter, D., George, S., Hattis, P., Singh, L., and Tavan, S., "Autonomous Guidance, Navigation, and Control of Large Parafoils," AIAA Paper 2005-1643, May 2005.

[4] Carter, D., George, S., Hattis, P., McConley, M., Rasmussen, S., Singh, L., and Tavan, S., "Autonomous Large Parafoil Guidance, Navigation, and Control System Design Status," AIAA Paper 2007-2514, May 2007.

[5] Jann, T., "Advanced Features for Autonomous Parafoil Guidance, Navigation and Control," AIAA Paper 2005-1642, May 2005.

[6] Carter, D., Singh, L., Wholey, L., Rasmussen, S., Barrows, T., George, S., McConley, M., Gibson, C., Tavan, S., and Bagdonovich, B., "Band-Limited Guidance and Control of Large Parafoils," AIAA Paper 2009-2981, May 2009.

[7] Slegers, N., and Costello, M., "Model Predictive Control of a Parafoil and Payload System," *Journal of Guidance, Control, and Dynamics*, Vol. 28, No. 4, 2005, pp. 816–821.
doi:10.2514/1.12251

[8] Kaminer, I., and Yakimenko, O., "Development of Control Algorithm for the Autonomous Gliding Delivery System," AIAA Paper 2003-2116, May 2003.

[9] Calise, A., Preston, D., and Ludwig, G., "Modeling for Guidance and Control Design of Autonomous Guided Parafoils," AIAA Paper 2007-2560, May 2007.

[10] Jann, T., and Strickert, G., "System identification of a Parafoil-Load Vehicle–Lessons Learned," AIAA Paper 2005-1663, May 2005.

[11] Yakimenko, O., and Statnikov, R., "Multicriteria Parametrical identification of the Parafoil-Load Delivery System," AIAA Paper 2005-1664, May 2005.

[12] Yakimenko, O., "On the Development of a Scalable 8-DoF Model for a Generic Parafoil-Payload Delivery Systems," AIAA Paper 2005-1665, May 2005.

[13] Calise, A., and Preston, D., "Approximate Correction of Guidance Commands for Winds," AIAA Paper 2009-2997, May 2007.

[14] Slegers, N., Beyers, E., and Costello, M., "Use of Variable Incidence Angle for Glide Slope Control of Autonomous Parafoils," *Journal of Guidance, Control, and Dynamics*, Vol. 31, No. 3, 2008, pp. 585–596.
doi:10.2514/1.32099

[15] Berland, J., Barber, J., Gargano, B., and Bagdonovich, B. P., "Autonomous Precision Delivery of 42,000 Pounds (19,000 kg) Under

One Parachute," AIAA Paper 2009-2928, May 2009.

[16] Lissaman, P., and Brown, G., "Apparent Mass Effects on Parafoil Dynamics," AIAA Paper 93-1236, May 1993.

[17] Chui, C. K., and Chen, G., *Kalman Filtering with Real-Time Applications*, 3rd ed., Springer–Verlag, New York, 1999, Chap. 8.

[18] Iacomini, C. S., and Cerimele, C. J., "Lateral-Directional Aerodynamics from a Large Scale Parafoil Test Program," AIAA Paper 99-1731, Jun. 1999.

[19] Jann, T., "Aerodynamic Model identification and GNC Design for the Parafoil-Load System ALEX," AIAA Paper 2001-2015, May 2001.

[20] Murray, J., Sim, A., Neufeld, D., Rennich, P., Norris, S., and Hughes, W., "Further Development and Flight Test of an Autonomous Precision Landing System Using a Parafoil," NASA TM-4599, Jul. 1994.

[21] Madsen, C. M., and Cerimele, C. J., "Flight Performance, Aerodynamics, and Simulation Development for the X-38 Parafoil Test Program," AIAA Paper 2003-2108, May 2003.

[22] "Final Report: Development and Demonstration of a Ram-Air Parafoil Precision Guided Airdrop System, Vol. 3," Draper Lab., Army Contract DAAK60-94-C-0041, National Soldier Center, Oct. 1996.

[23] Dellicker, S., Benney, R., and Brown, G., "Guidance and Control for Flat-Circular Parachutes," *Journal of Aircraft*, Vol. 38, No. 5, October 2001, pp. 809–817.
doi:10.2514/2.2865

[24] "Military Standard, Flying Qualities of Piloted Aircraft," MIL-STD-1797A, Jan. 1990.